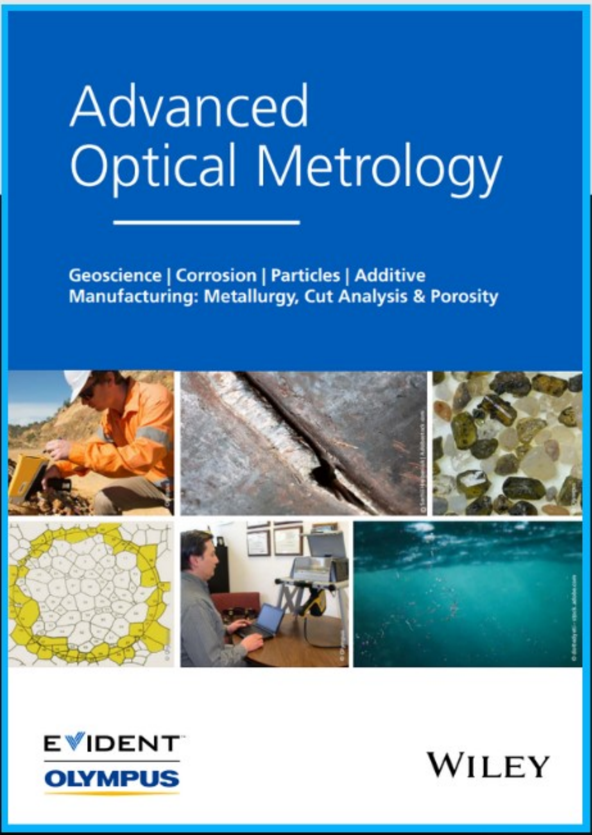

ADVANCED FUNCTIONAL MATERIALS
www.afm-journal.de

Giant Polarization in Quasi-Adiabatic Ferroelectric Na^+ Electrolyte for Solid-State Energy Harvesting and Storage

*Manuela Carvalho Baptista, Hesham Khalifa, Adão Araújo, Beatriz Arouca Maia, Manuel Souto, and Maria Helena Braga**

The advent of new solid-state energy storage devices to tackle the electrical revolution requires the usage of nonlinear behavior leading to emergent phenomena. The ferroelectric analyzed herein belongs to a family of electrolytes that allow energy harvesting and storage as part of its self-charging features when thermally activated. The $Na_{2.99}Ba_{0.005}ClO$ electrolyte shows quasi-adiabatic behavior with a continuous increase in polarization upon cycling, displaying almost no hysteresis. The maximum polarization obtained at a weak electric field is giant and similar to the remanent polarization. It depends on the temperature with a pyroelectric coefficient of 5.37 C m^{-2} $°C^{-1}$ from −5 to 46 °C. The emergence occurs via negative resistance and capacitance. The glass transition is found to have its origins in the sharp depolarization at 46 – 48 °C. Above −10 °C, at ≈ −5 °C, another thermal anomaly may rely on the topologic characteristics of the $A_{3-2x}Ba_xClO$ (A = Li, Na, K) glass electrolytes enabling positive feedback of the current of electrons throughout the surface of the inner cell. The phenomena may pave the way toward a better understanding of dipolar nanodomain fragile glasses with exceptional ferroelectric characteristics to architect energy harvesting and storage devices based on multivalent thermally activated Na^+-ion-ion electrolytes.

1. Introduction

The high level of carbon emissions from non-renewable energy, such as fossil fuels, has many detrimental effects, i.e., climate change and global warming, hazardous waste, and destruction of habitats resulting in biodiversity loss. At the same time, concerns regarding fossil energy supply are increasing quickly in countries with high energy consumption, industrial activities, and rapid globalization. One way to curb this impact is to transition from fossil fuels to renewable energy[1,2]. Renewable energies are sourced from natural processes such as sunlight, wind, and waves which can be replenished and are environmentally friendly sources of energy[3,4]. Renewable energy, especially solar and wind energy, strongly depends on local weather and climate conditions with intermittent and fluctuating features. To filter these variabilities, batteries have been broadly used as one of the potential solutions which can store energy during low-demand situations and work as an alternative power generation source by discharging the stored energy during peak demand[5,6].

Battery usage has rapidly increased due to the fast-growing mobile electronic equipment industry in recent decades. Standardization and in-depth studies toward reliable and low-cost high energy density batteries with high eco-friendly properties are necessary for today's life[7]. Lithium-ion batteries (LIB) have revolutionized the trend for all electrical applications due to their high energy and power density combination. However, these batteries have quite a few limitations, such as not charging fast enough, having a flammable electrolyte, and having cathodes that tend to reach their theoretical capacity limit[8]. Researchers worldwide are trying to optimize batteries in terms of efficiency and using sustainable and environmentally friendly materials.

M. C. Baptista, H. Khalifa, B. A. Maia, M. H. Braga
Engineering Physics Department, Engineering Faculty
University of Porto
Porto 4200–465, Portugal
E-mail: mbraga@fe.up.pt

The ORCID identification number(s) for the author(s) of this article can be found under https://doi.org/10.1002/adfm.202212344.

DOI: 10.1002/adfm.202212344

H. Khalifa
Department of Physics, Faculty of Science
Damanhour University
Damanhur 22511, Egypt

A. Araújo
Norleq – Equipamentos e Serviços, Lda.
Hipercentro, F, Porto 4200–279, Portugal

B. A. Maia, M. H. Braga
LAETA – INEGI
Institute of Science and Innovation in Mechanical and Industrial Engineering
Porto 4200–465, Portugal

M. Souto
Department of Chemistry, CICECO-Aveiro Institute of Materials
University of Aveiro
Aveiro 3810-393, Portugal

Solid-state electrolytes (SSEs) have been attracting significant attention due to their advantages, such as non-flammability, higher thermal stability, no leakage risk, and non-volatile materials; SSEs also demonstrate better mechanical properties and higher electrochemical window of stability[9] besides a lower predisposition to form dendrites. These latter features facilitate the use of alkali metal anodes and a wider variety of cathodes.

All-solid-state electrolytes are categorized into inorganic solid electrolytes (ISEs), polymer solid electrolytes (PSEs), and organo-inorganic hybrid electrolytes.[10–13] ISEs, such as oxide-based electrolytes, may have good ionic conductivity when compared to organic electrolytes.[14] In this group of electrolytes, those that add being ferroelectrics stand out because they present exciting properties, namely a high dielectric constant that coexists with a suitable alkali-ion conductivity.[15] Herein, we show that $Na_{2.99}Ba_{0.005}ClO$ glass-electrolyte belongs to the family of relaxor-ferroelectric oxides with low resistance (high ionic conductivity), self-charge (negative resistance)[16], and self-cycling behavior.[8,17] The electrolyte's thermal behavior and thermodynamic, ionic, and electrical properties are multi-coupling features, affecting different parameters related to the battery, such as safety, cycle life, and electrochemical reactions.[18–20] Investigation of the thermal behavior of the electrolyte is crucial to improve its performance within the cell.[9] To the best of our knowledge, this is the first time that the polarization process and thermodynamic properties of $Na_{2.99}Ba_{0.005}ClO$ solid electrolyte have been studied, paving the way for the design of safer and more efficient Na^+-based solid electrolytes.

1.1. Ferroelectric Relaxor

Dielectric bulk ceramics are categorized into groups such as linear dielectrics, ferroelectrics, relaxor ferroelectrics, and antiferroelectrics.[21–26] Ferroelectrics, antiferroelectrics, and relaxor ferroelectrics exhibit more significant potential differences and energy density than conventional linear dielectrics[27–32] when polarized. Equations 1–3 can be used to compute the energy storage density (W), recoverable energy storage density (W_{rec}), and energy storage efficiency (η) of dielectric bulk ceramics.[21,22,33]

$$W = \int_{0}^{P_{max}} \mathbf{E}.d\mathbf{P} \tag{1}$$

$$W_{rec} = \int_{P_r}^{P_{max}} \mathbf{E}.d\mathbf{P} \tag{2}$$

$$\eta = \frac{W_{rec}}{W} \tag{3}$$

Where **P** is the polarization vector, P_r the residual polarization, P_{max} is the maximum polarization a,nd, and **E** the applied electric field.

Significant dielectric breakdown strength (E_b), high P_{max}, and low P_r are all necessary to build dielectric bulk ceramics with both high W_{rec} and high η according to Equations 1–3. Because of their mild E_b, large P_{max}, and low P_r dielectric bulk ceramics, antiferroelectrics, and relaxor ferroelectrics are likely the best candidates for electrical energy storage devices [21–23]. Some properties of antiferroelectrics restrict their technological uses, such as limited usage mainly due to hazardous lead nature and shorter life cycles, i.e., degradation of antiferroelectrics behavior with time [34].

Ferroelectric ceramics are among the essential functional materials in current technology. A large number of polar nanodomains/islands known as polar nanoregions (PNRs)[35,36] are known as relaxor ferroelectric after E. Cross's studies in 1987.[37] Both regular and relaxor ferroelectric materials have a persistent dipole moment; however, standard ferroelectric dipoles typically have a micro-length scale, while relaxor ferroelectric have a nano-length scale, requiring less energy to align. As a result, the latter ferroelectrics have much higher dielectric constants, propitiating very high specific capacitance with significant advantages in energy storage applications. Notice that relaxor ferroelectric materials have high-density discharge energy rates due to their needle-like low surface hysteresis curve with high-saturated polarization and low residual polarization (see **Figure 1**; Figure S1, Supporting Information).

Several models for describing dielectric anomalies in relaxor ferroelectrics are offered, leading to the formulation of the notion of the genesis of dynamic and the creation of PNRs.[37–40] The primary component associated with producing PNRs & PNRs has been linked to the appearance of inherent inhomogeneity in the material due to compositional fluctuation at the crystallographic sites and structural variation of the unit cell. N. Qu et al.[41] investigated the development of ferroelectric domains containing PNRs in ferroelectric ceramics. As the nanodomain fraction increases, the ferroelectric hysteresis loop grows narrower (low hysteresis loss). This phenomenon arises from a decrease in the interaction strength order parameters (dipole moments).

When in the presence of an output electric field, both the ferroelectric domains and the nanodomains reorder and then turn in the direction of the electric field. At zero field, practically all domains change back to their original state, but a portion of the ferroelectric domains remain aligned. The P_r value can be marginally small compared to conventional ferroelectrics, as shown in the schematic representation in Figure S1 (Supporting Information). Another disadvantage of relaxor ferroelectrics with ferroelectric domains and nanodomains is their substantial dielectric nonlinear function, which causes the polarization value to reach P_{max} at a low electric field.[42] As a result, these dielectric ceramics often have high P_{max}, moderate P_r, and strong dielectric nonlinearity, with moderate W_{rec} and moderate η.[43]

Many materials exhibiting relaxor ferroelectric activity are currently accessible in different crystal structures, such as perovskite, layer perovskite, tungsten bronze structure, and ferroelectric polymers. These materials have high dielectric constants and nearly little residual polarization, resulting in substantially better energy densities and charge-discharge efficiencies than regular ferroelectrics in energy storage systems.[44] If the ferroelectric domains are split apart, solitary nanodomains and PNRs, as shown in Figure 1, are formed, characterizing the resulting relaxor ferroelectrics. In PNRs relaxor ferroelectric, the type and size of ferroelectric domains are strongly influenced by external parameters (e.g., electric field, temperature, stress, etc.) and, as a result, alter their physical

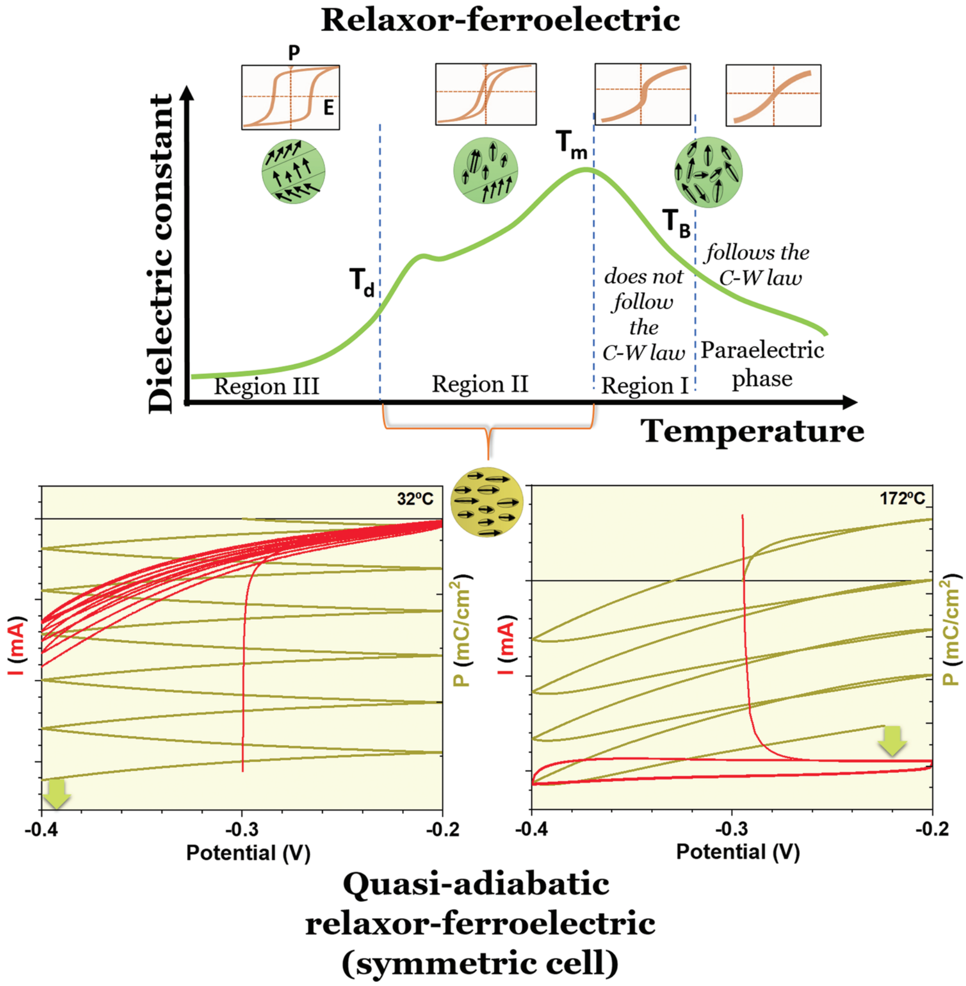

Figure 1. The temperature-dependent dielectric constant of a relaxor ferroelectric is linked to different characteristic temperatures that delimitate the assigned regions. T_d – depolarization temperature; T_m – maximum dielectric permittivity; T_B – Burn temperature. Below are the different behavior highlights for the newly characterized quasi-adiabatic relaxor ferroelectric Na$^+$-electrolyte with giant remanent polarization capabilities.

properties.[45] Compared to regular ferroelectric domains, large P_{max} under a low electric field, is more difficult to achieve due to the inability to generate long-range ferroelectric ordering due to the elevated local random inner electric field.[44] However, under a strong applied electric field, PNRs can progressively change into long-range orders, which promote linear polarization behavior and a high P_{max}. More interestingly, after eliminating the electric field, the long-range orders can flip back to their previous condition, resulting in little P_r. Furthermore, the PNRs promote thin $P-E$ loops and high E_b because of their high dynamics and minimal hysteresis loss.[35,36] Due to high P_{max}, low P_r, high E_b, and reduced hysteresis $P-E$ loops, relaxor ferroelectrics with PNRs are extremely promising for achieving both large W_{rec} and high η.[35,36]

Superparaelectrics behave very similarly to relaxor ferroelectrics but are defined as non-interacting spherical nanoparticles; in other words, they contain nanodomains in a non-interacting matrix.[46]

As a result of the preceding discussion, it is possible to infer that customizing the domain size to the coexistence of nanodomains or PNRs may be a valuable method for achieving large W_{rec}, high η, and excellent thermal stability in lead-free bulk ceramics.

Unlike regular ferroelectrics with long-range ferroelectric orders, relaxor ferroelectrics may be considered macroscopically paraelectric, with almost no spontaneous polarization at zero electric fields.[25,47,48] Moreover, relaxor ferroelectrics have unusual properties such as frequency-dependent dielectric constants over a wide temperature range, ultrahigh piezoelectric response, and massive electrocaloric effect; they are ideal for acoustic sensing, micropositioners, actuators, and electrocaloric cooling devices.[49–52]

Herein we show that $Na_{2.99}Ba_{0.005}ClO$ is a ferroelectric with different features; it shows all the above properties shown for relaxor ferroelectrics or superparaelectrics, except for a giant spontaneous polarization at zero electric fields P_r that increases continuously upon cycling, leaving no "forbidden" or unrecovered energy regions. In fact, Na$^+$-electrolyte is not a regular ferroelectric, a relaxor ferroelectric, or even a superparaelectric.[46]. Still, it shows characteristics of all ferroelectrics/superparaelectrics (Figure 1). Just below the depolarization temperature, the I–V curve shows a similar shape to the P–V's of a ferroelectric relaxor or a superparaelectric. This behavior indicates that the Na^+-electrolyte is a chemical inductor [53,54], showing a negative resistance and capacitance that contribute to continuous charge induction and storage upon cycling. Above T_d, the $Na_{2.99}Ba_{0.005}ClO$ electrolyte in a symmetric cell behaves as a quasi-adiabatic ferroelectric, with polarization happening very quickly in PNRs, very high $|P_r| \approx P_{max}$, $|E_c| \approx E_{appliedmax}$, with a polarization per cycle raising $\Delta P = 2.8$ mC cm^{-2} per cycle or $\Delta U = 0.334$ mJ cm^{-2} per cycle with amplitude $\Delta V = \pm 0.2$ V, at 20 °C, which, in fact, translates in a capacitance increase of $\Delta C = 7$ mF cm^{-2} per cycle.

1.2. Temperature-Dependent Dielectric Constant of a Relaxor-Ferroelectric

The relaxor ferroelectric temperature-dependent dielectric constant or real relative permittivity (ε_r' vs T) gives extensive information about the dynamic and creation of PNRs, as shown in Figure 1.

The ε_r' versus T curve contains information with essential characteristics identified by E. Cross[37] for the first time; relaxor ferroelectrics are characterized by a broad and smeared maximum in the temperature-dependent dielectric constant (ε_r'), whose positions shift to higher temperatures as the frequency of the applied electric field increases[55,56]; this maximum corresponds to a diffuse phase transition.[35]

Figure 1 illustrates the three characteristic temperatures in the real relative permittivity, or dielectric constant, versus temperature, namely: T_d (depolarization), T_m (maximum), and T_B (Burn). 1) T_d is defined as the temperature corresponding to the sharpest decline in remanent polarization; 2) T_m correlates to the maximum dielectric constant, yet not giving rise to a macroscopic symmetry break (structural transition) near this temperature; 3) the temperature-dependent dielectric constant does not obey the Curie–Weiss (C-W) law closer to T_m; and, finally, 4) paraelectric phase behavior above the Burn's temperature (T_B)[57] with zero net dipole moment (randomly oriented dipole moments) where the dielectric properties obey the Curie–Weiss law.

It is also possible to analyse Figure 1 and Figure S1 (Supporting Information) by taking into account the three different polar states, as they are dependent on the dielectric behaviors.[35,37,56,58,59]

Region I between T_m and T_B: the formation of PNRs begins during cooling from T_B to T_m; the temperature range at which the ε_r' versus T curve does not follow the C–W law. T_B represents the phase change from paraelectric to ergodic relaxor. Further temperature reduction promotes the creation of PNRs, which are then maximum in volume at approximately the maximum dielectric constant's temperature (T_m) with a broad dispersive peak. This region represents an electrostrictive region with a chemically ordered region with no macro-scale ferroelectric domain; some polar regions gradually emerge. At this condition, PNRs are highly dynamic, and thermal fluctuations can switch their polar vectors; their interface within the matrix is movable. Therefore, the region I can be illustrated by little or no hysteresis. **Region II** between T_d and T_m: on cooling to a temperature lower than T_m, the nanoscale polar regions' dynamics slow down, freezing out into macro-domain regions. With the decreasing temperature, the polar regions grow and cluster. From the temperature where dielectric dispersion can be observed to T_d, the relaxor ferroelectrics exhibit hysteresis, which becomes more pronounced with decreasing temperature. **Region III** below T_d: when the temperature is low enough $T \leq T_d$, relaxors can enter a dipolar-glass state or mixed ferroelectric-glass state, where long-range ferroelectric domains can be achieved by electric-field poling. The macro-domain region becomes more stable, which results in a large spontaneous polarization and piezoelectric effects with a significant remanent strain that can be illustrated by large hysteresis.

The quasi-adiabatic ferroelectric discussed herein, shows features of all the three previous regions, not being fully identified with any of them. The properties shown remit to a PNR ferroelectric relaxor with 1D chains[17] that preserve the long-range polarization order leading to an extremely high P_r while not conducing to dissipative effects under the action of a variable applied electric field, as the chains' ends polarization is easily altered.

1.3. Modulated Differential Scanning Calorimetry (MDSC)

Modulated DSC (MDSC) or Temperature Modulated DSC (TM-DSC) strengthens the investigation of differential thermal analysis.[60] This method was developed by Reading and Hourston, and TA Instruments that patented this technique[61], where a linear heating method with a superimposed sinusoidal oscillation is enforced on the sample, resulting in a cyclic heating profile. MDSC demonstrates several advantages, from separating kinetic and heat capacity components to enhanced identification of glass transitions, precise heat capacity measurements, and refined separation of overlapped transitions.[62]

The theoretical basis of the MDSC technique[63–66] is described as follows,

$$\frac{dH}{dt} = C_{P'}\frac{dT}{dt} + f(T,t) \tag{4}$$

where $\frac{dH}{dt}$ is the total heat flow rate (mJ s^{-1}), $C_{P'}$ is the heat capacity, $\frac{dT}{dt}$ is the temperature rate (°C min^{-1}), and $f(T, t)$ is the heat flow variation behavior of the sample, which is a function of temperature and time.

The total heat flow is the sum of all heat flows at any time and temperature. MDSC determines not only the total heat flow, such as a conventional DSC, but also allows to calculate the heat flow of individual transitions. Equation 4 can be rewritten as follows, *Total Heat Flow = Reversing Heat Flow + Non − reversing Heat Flow*. MDSC can determine these three signals to better interpret complex transitions in the sample. The total heat flow signal $\left(\frac{dH}{dt}\right)$ is obtained from the average value of the determined modulated heat flow signal by Fourier transform analysis. The second signal, the reversing heat flow, is obtained from reversing heat capacity signal by the following equation, *Reversing Heat Flow = Reversing Heat Capacity × Average Temperature Rate*. Reversing Heat Capacity can be calculated by the equation,

$$C_{P',\,rev} = K_{C_{P'}\,rev} \times \frac{\text{Heat Flow Amplitude}}{\textit{Temperature Rate Amplitude}} \tag{5}$$

where $K_{C_{P}'\,rev}$ is the calibration constant for the reversing heat capacity. Sapphire is used as a reference to obtain $K_{C_{P}'\,rev}$. Finally, the non-reversing heat flow signal is obtained by subtracting the reversing heat flow signal from the total heat flow signal.

Several research studies include the MDSC technique, among them polymeric materials for which MDSC is used to disentangle the often complex phase transitions, such as the glass transition[67–75]. MDSC is also valuable for understanding the behavior of metallic glasses of $Al_{89}Ni_6La_5$, $Al_{87}Ni_6La_7$, and $Al_{87}Ni_5La_7M1$ (M = Ag, Cu)[76]. It is highly effective to determine the specific heat capacity ($C_{P'}$) of the epoxy resin[77]. Solid electrolytes' thermodynamic properties of AgI and Ag_2Se[78], $(Ag_2S)_x(As_2S_3)_{1-x}$ glasses[79], $Li_{1.5}Al_{0.5}Ge_{1.5}(PO_4)_3$ (LAGP), $Li_{6.4}La_3Zr_{1.4}Ta_{0.6}O_{12}$ (LLTZO), as well as Li^+-sulfides and halides[80], the effect of Fe_2O_3 fillers into a caesium-based solid electrolyte[81], polyethylene glycol (PEG)–α-cyclodextrin (αCD) complex and poly(acrylic acid) (PAA) electrolyte[82], and the influence of Li_2O content in $40B_2O_3$-$20CdO$-$(40\text{-}x)Bi_2O_3$-xLi_2O glasses[83] were also studied using MDSC. Here we compare the MDSC reversing heat capacity with the heat capacity obtained, also experimentally, by cyclic voltammetry and, theoretically, with ab initio simulations including phonons at elevated temperatures. We demonstrate that the depolarization leads to the glass transition.

2. Results and Discussion

As discussed in the introduction, outstanding features can be achieved with relaxor ferroelectric materials and superparaelectrics, even though this field is still in its infancy.

Herein, for the first time, the concept of PNRs inside the relaxor ferroelectric $Na_{2.99}Ba_{0.005}ClO$ solid-state electrolyte is employed to characterize quasi-adiabatic ferroelectrics. Thermodynamic characterization of the PNRs is also established for the first time.

Figure 2a shows the temperature-dependent dielectric constant, ε_r' versus T, and Figure 2b the ionic conductivity σ versus T of $Na_{2.99}Ba_{0.005}ClO$ ferroelectric glass electrolyte from 25 to 172 °C. The depolarization temperature is T_d ~ 47 °C, T_m ~ 170 °C, and T_B is not identified within the measured temperature range. Region II is observed for the ε_r' versus T curve of $Na_{2.99}Ba_{0.005}ClO$; therefore, one may argue that $Na_{2.99}Ba_{0.005}ClO$ is an electrolyte showing relaxor ferroelectric features, although exhibiting differences. All regions are highly dependent on frequency. No region may be observed where the dielectric constant is not frequency-dependent (Figure 2a); conversely to regular ferroelectrics, region III is the most frequency-dependent region. This characteristic may be attributed below the glass transition (<61 °C), to the maximum polarization being highly dependent on the natural frequency requiring resonance from the applied field. Above this temperature, a broad range of frequencies replaces this characteristic frequency, as the liquid state is more disordered, and the polarization becomes more dependent on the temperature to achieve different minimal states on the fragile glass landscape, as discussed hereafter.

The ionic conductivity shows similar features to the dielectric constant. However, not strictly at the same temperatures (Figure 2b). The ionic diffusion is related to polarization and vice-versa, as the polarization is propitiated by ionic conduction but may also restrict it (especially in polar asymmetric cells). At the same time, ionic/dipolar relaxation follows in decreasing the internal energy.

In heterogeneous dynamics of amorphous/glass materials[84], their correlated domains relax following an exponential tendency and almost independently of each other. This scenario configures that of a superparaelectric with nanodomains with immense dielectric capabilities[46], for achieving high energy density and high efficiency. In other words, nanodomains forming chains parallel to the applied electric field allow for large polarization, keeping long-range order and low hysteresis while having ends easily polarization reversible. Here we found very low to no hysteresis in the polarization versus applied potential, in ($P - V$) plots, dependent on the applied rate, temperature, and the application of ferroelectric relaxor/superparaelectric

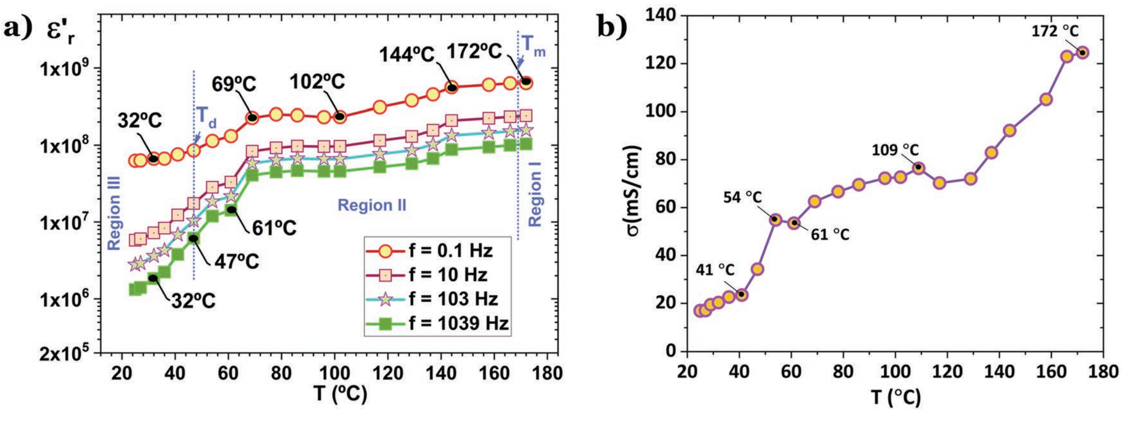

Figure 2. A frequency and temperature-dependent dielectric constant and ionic conductivity of relaxor ferroelectric $Na_{2.99}Ba_{0.005}ClO$ solid electrolyte, obtained by EIS with Au/$Na_{2.99}Ba_{0.005}ClO$/Au cells. a) dielectric constant; b) ionic conductivity. Note: T_d – depolarization temperature; T_m – maximum dielectric permittivity; the three regions are delimited by the assigned temperatures.

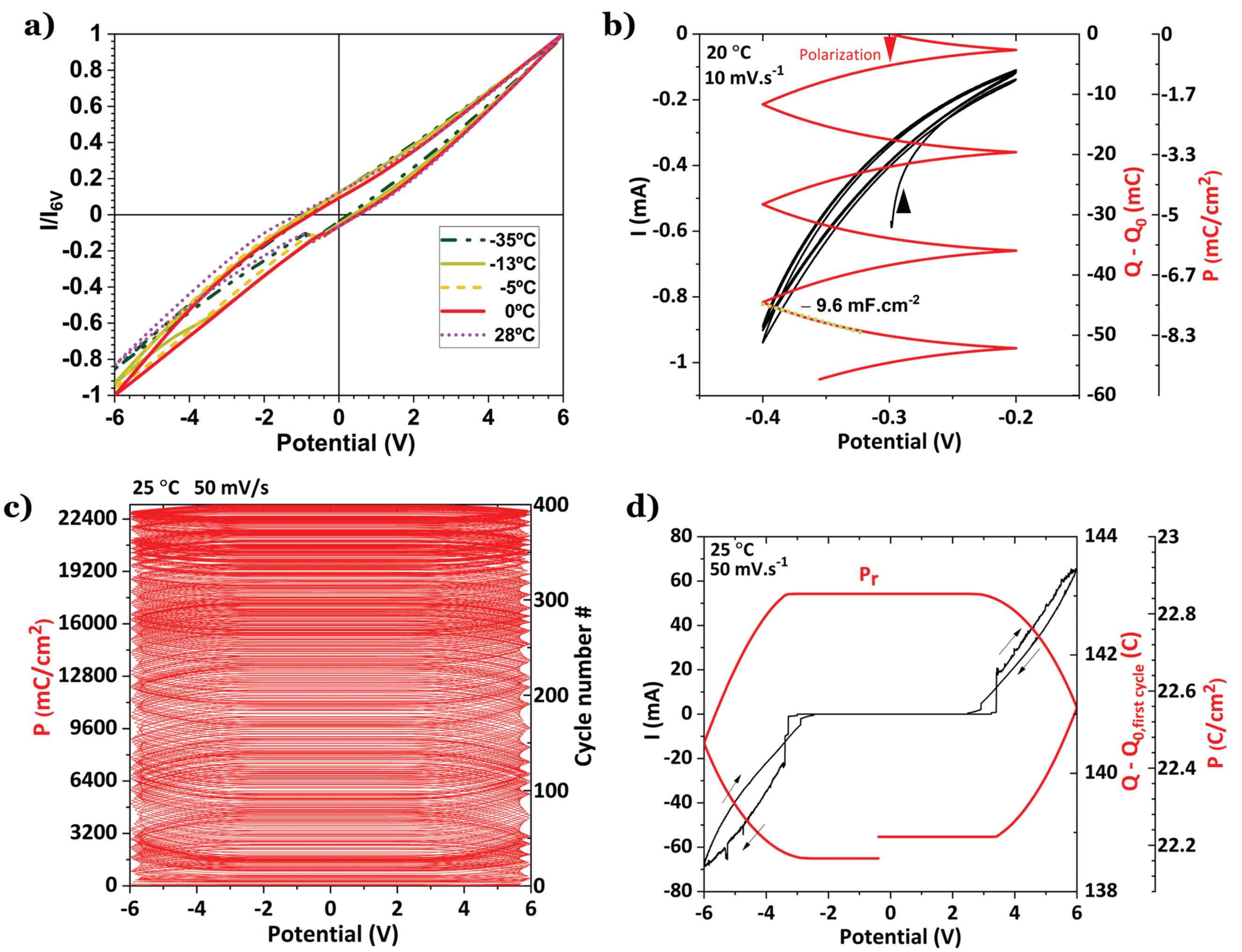

Figure 3. Temperature and rate-dependent *I*–*V* of relaxor ferroelectric $Na_{2.99}Ba_{0.005}ClO$ solid electrolyte; a) I–V at different temperatures normalized for I(6 V) showing the shape and the variation of the applied potential for I = 0 mA (dV/dT = 50 mV s^{-1}); b) to d) *I*–*V* and *Q*–*V* showing quasi-adiabatic polarization at 20 and 25 °C; in d) detail of cycle 400 in (c) showing *Q*–*V* and *I*–*V* plots. Note: self-polarized electrolyte (symmetric cells) Au/$Na_{2.99}Ba_{0.005}ClO$/Au ($A \approx 6$ cm^2, $d \approx 2$ mm) showing negative resistance and negative capacitance capable of increasing the polarization of the electrolyte for more than 400 cycles, corresponding to $\langle \Delta C \rangle$ = 2.3 mF cm^{-2} per cycle. In the *I*–*V* plot of d), the steps from 2 to 4 V and −2 to −4 V are quantum Josephson junctions' excitation-like phenomena.

polarization bias, i.e., the use, or not, of an asymmetric cell (**Figure 3**). In fact, there are no "forbidden" or lost energy with cycling, with continuous raise of the capacitance corresponding to $\langle \Delta C \rangle$ = 2.3 mF cm^{-2} per cycle as demonstrated in Figure 3b,c.

Figure 3a shows the shape of the *I*–*V* plot normalized to $I/I(6\ V)$ to highlight the potential at 0 mA. Essentially, the shape of the *P*–*V* (or *P*–*E*) curve of a regular relaxor ferroelectric corresponds to the shape of the *I*–*V* curve of a quasi-adiabatic ferroelectric as the one analyzed in this study; reinforcing the effects of the negative resistance, $-\ r$, and capacitance, $-\ C$, made possible by an adiabatic process, and leading to self-charge[53,54] $\left(\left\{\frac{Q}{C}\right\}_{\text{relaxor}} = \{-rI\}_{\text{quasi-adiabatic}}\right)$. The details of cycle 400 in Figure 3d shows a giant gain in the polarization of an inductor-like or negative resistor circuit element Au/$Na_{2.99}Ba_{0.005}ClO$/Au. The discontinuities observed in the *I*–*V* plot, from 2 to 4 V, are quantum Josephson junctions like Shapiro steps for a supercurrent across a weak link carried by exciton states[85] compatible with 1D transport.

The *P*–*V* of $Na_{2.99}Ba_{0.005}ClO$, from −35 to 28 °C, corresponds to a "rectangle" shape formed by two quasi-parallel regions of positive capacitance, with two almost quasi-parallel regions of negative capacitance. The edges of the rectangle are P_{max} and $P(V_{max})$, and P_{min} and $P(V_{min})$, where V_{max} and V_{min} were chosen upon experiment design (**Figure** 4a; Figure S3, Supporting Information). Poled samples in asymmetric cells behave very similarly to non-poled samples from −35 to −5 °C (Figure 3 and Figure 4b). Above 0 °C, negative resistance (differential and static) and negative differential capacitance are observed from ≈0.2 to ≈0.9 V, corresponding to the positive feedback of electron current through the surface of the glass-electrolyte in the inner cell. The current of electrons tunnels from the ferroelectric electrolyte's surface to the negative electrode while the cell is set to discharge, increasing the current's intensity. When the cell is

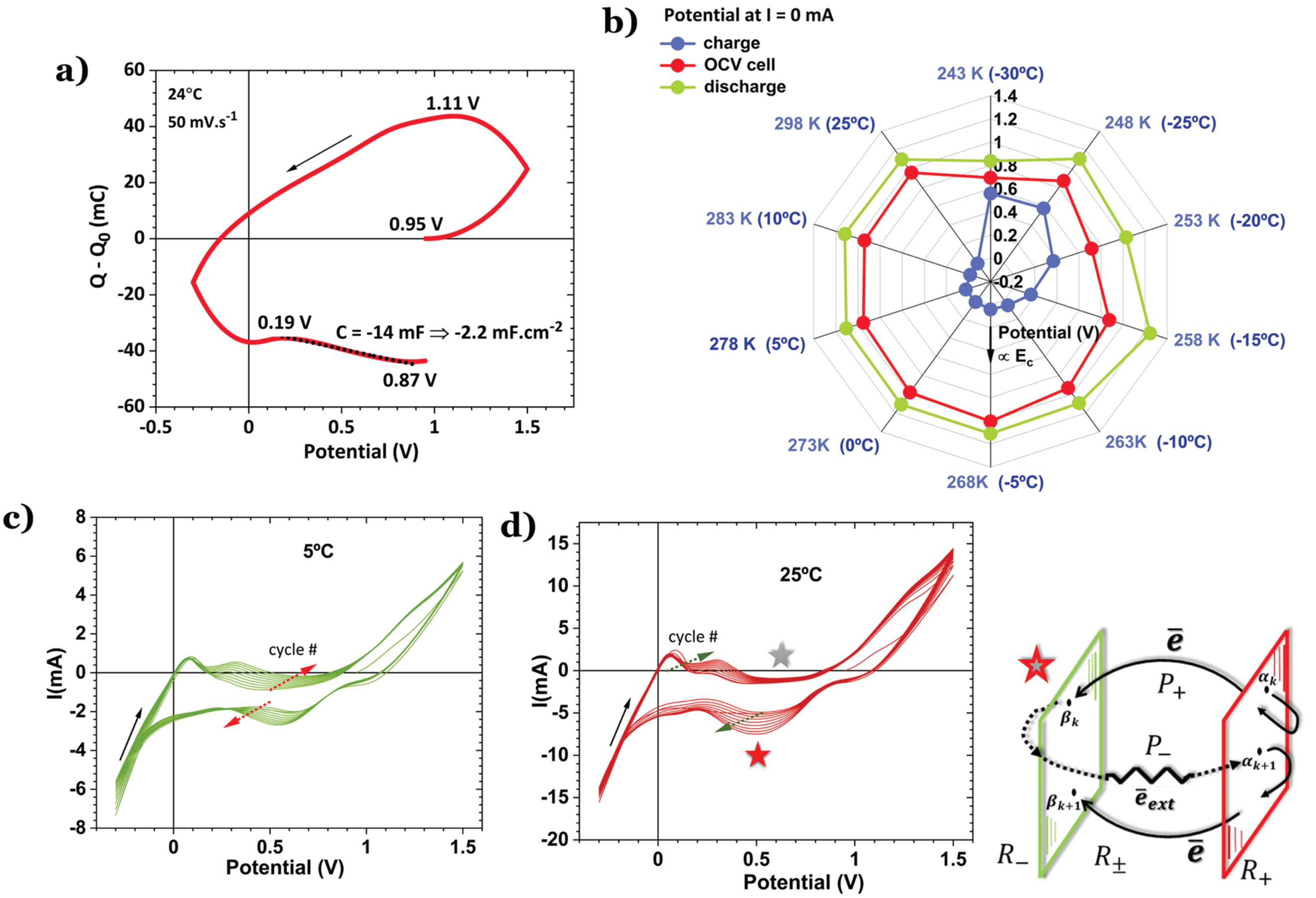

Figure 4. Temperature-dependent *P*–*V* and *I*–*V* relaxor-ferroelectric $Na_{2.99}Ba_{0.005}ClO$ glass-electrolyte. Capacity versus potential (50 mV s^{-1}, A = 6.25 cm^2): a) *Q*–*V* at 24 °C; b) Potential versus temperature for 0 mA showing the stability of the behavior above −5 °C; c) *I*–*V* at 5 °C; d) I–V plot at 25 °C, showing negative resistance from 0.3 to 0.85 V. Right side of d), partitioning of the state space and the Poincaré maps correspondent to positive feedback (P_- is the external circulation of the current of electrons, P_+ is the internal circulation of the current of electrons, $\overline{e}$, while the cell was set to discharge, red star; − P_- is the external circulation of current, P_+ is the internal circulation of current, *I*, while the cell was set to charge; grey star)[93,53]. Note: the relaxor-ferroelectric electrolyte is polarized by an asymmetric cell, Zn/$Na_{2.99}Ba_{0.005}ClO$/Cu (A ≈ 6 cm^2, d ≈ 4 mm).

set to charge, the current decreases and may become negative when the number of electrons circulating from the electrolyte's surface to the negative electrode is higher than the number of electrons that reach the negative electrode through the external circuit (Figure 4c,d). Once the latter happens, the cell discharges while set to charge, and the static resistance is then − *r*.

The negative differential resistance in an *I*–*V* plot was first observed with a tunnel (Esaki) diode[86,87,88]. Nonetheless, the negative current is an original feature of these cells not seen in the tunnel diodes, although observed in the bulk photovoltaic effect (BPE) when the polarization of the light is parallel to the c-axis of a semiconductor such as a $BaTiO_3$ ferroelectric single crystal[89]. The negative current in the BPE is designated shift current[90]. In the power-generating region of the *I*–*V* plot of these photovoltaics, electrons move in the opposite spontaneous direction predicted by the drift-diffusion equation, i.e., electrons move toward a higher chemical potential, or holes move toward a lower chemical potential. In this region, the negative resistance and current of the photovoltaics demonstrating BPE[91,92] behave just like the Zn/$Na_{2.99}Ba_{0.005}ClO$ electrolyte/Cu in Figure 4. However, in or case, the process does not require a pump such as in the BPE.

In fact, as demonstrated in Figure 4b, the charging potential at 0 mA markedly increases from −30 to −5 °C as observed in the CV analysis (*I*–*V* plot) of the Zn/$Na_{2.99}Ba_{0.005}ClO$/Cu asymmetric cell.

The lack of hysteresis configures an adiabatic cycling process at a constant temperature *T*. In Figure 3b, we show adiabatic processes propitiating regions where the differential resistance and capacitance are negative, which are also observed in Figure 1 and Figure 4a,c,d, with the corresponding schematics of the process presented on the right side of Figure 4d (Poincaré double maps[93,53]). It is noteworthy to highlight that other ferroelectrics, such as[94], show maximum capacitances $C_{max} \approx 0.1\ \mu F\ cm^{-2}$. Here we show capacitances of $C_{max} \approx 15\ F\ cm^{-2}$ at 25 °C.

When the reversibility of the processes involved in the previous discussions is assumed ($T\partial S = Q'$) at a constant volume ($\partial V' = 0$), where *S* is the entropy, *Q*′ is the heat, and *V*′ the volume. The Helmholtz free energy *F* is then expressed as,

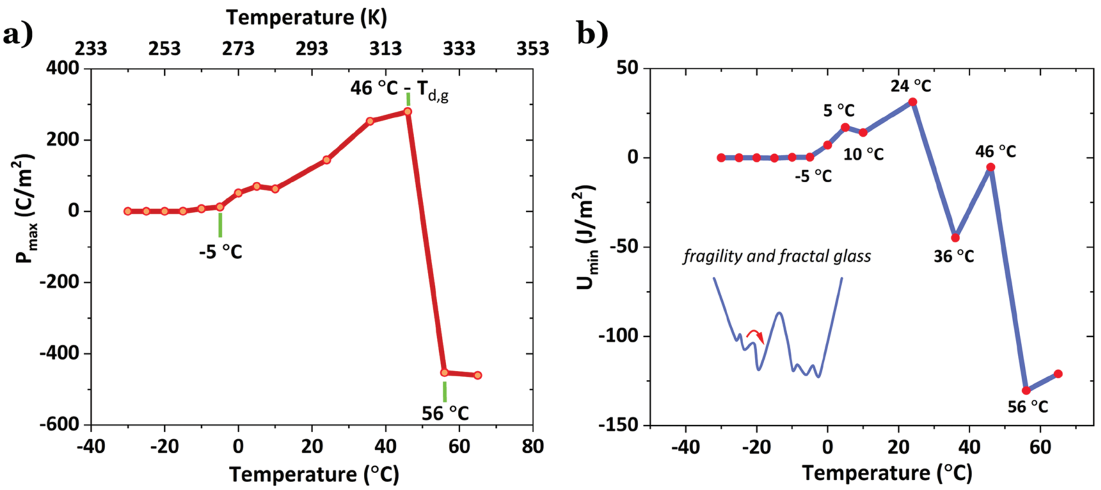

Figure 5. Temperature-dependent a) maximum polarization showing a distinct phase transition from 46 to 56 °C and b) minimum internal potential energy for the quasi-adiabatic ferroelectric $Na_{2.99}Ba_{0.005}ClO$ electrolyte. Both obtained by cyclic voltammetry (50 mV s^{-1}) at constant temperature with an asymmetric cell Zn/$Na_{2.99}Ba_{0.005}ClO$/Cu (A ≈ 6 cm², d ≈ 4 mm). Note: the pyroelectric coefficient, $\frac{dP}{dT} =$ 0.29 C m^{-2} °C^{-1} [−30 °C,−5 °C]; $\frac{dP}{dT} =$ 5.37 C m^{-2}.°C^{-1} [−5 °C,46 °C].

$$\partial F = \partial U - S\,\partial T - T\,\partial S = Q' - P'\partial V' + \partial W_e - S\,\partial T - T\,\partial S = \partial W_e \tag{6}$$

where U is the internal energy, P' the pressure, and W_e is the electrical work that will be determined directly from the $Q - Q_0$ versus V or P versus V, $\partial\, W_e = VdQ$. According to the Ginzburg–Landau-Devonshire (G-L-D) theory applied to devices[95], $\Delta F = \frac{a}{2}\,(T - T_0)P^2 + \frac{b}{4}P^4 + \frac{c}{6}P^6 - EP$ where a, b, and c are parameters, E the applied electric field, and T_0 the critical temperature. In a traditional ferroelectric, the critical temperature corresponds to the Curie temperature.

In the quasi-adiabatic ferroelectric electrolyte, bulk polarization is defined by the G-L-D theory; however, in an asymmetric cell, the surface's positive feedback current adds to the bulk polarization, and the cell's potential and output current reflect both phenomena. Therefore, the experimental data are a reflection of both components.

The calculation of P_{max} and $\partial\, U_{min} = \partial\, W_e = VdQ$ was performed based on the plots in **Figure 5**. From the latter, we obtain the pyroelectric coefficient $\frac{dP}{dT} =$ 0.29 C m^{-2}.°C^{-1} [−30 °C,−5 °C], $\frac{dP}{dT} =$ 5.37 C m^{-2} °C^{-1} [−5 °C,46 °C], which is minimum three orders of magnitude higher than $BaTiO_3$[96], PZTO[97], PVDF[98], and Glycolipids[99].

There is a flow of ions in the glass Na^+ – electrolyte at the depolarization temperature T_d, which corresponds to the sharpest decline in remanent/maximum polarization (Figure 5a). Approximately at the same temperature T_g, the transition from glass to supercooled liquid electrolyte, is likely boosted by the depolarization movement of the ions in the electrolyte. In fact, the polarization alters from positive to negative, even in a poled cell as shown in Figure 5a. The T_d temperature corresponds to a local maximum in the internal energy (Figure 5b). The internal energy versus temperature landscape shows possible minimum relative states as in a fragile fractal glass (basins).[100] The local minima at 36 °C and 56 °C correspond to approximately the onset and peak of the glass transition shown in **Figure 6** and Figures S4–S6 (Supporting Information), and they correspond to states that are thermally stabilized to minimal energy configurations.

The difference in heat capacity due to spontaneous depolarization,

$$\Delta C_{P'} \approx \Delta C_{V'} \approx \left(\frac{\partial W_e}{\partial T}\right) = \frac{\partial}{\partial T}\int VdQ \tag{7}$$

where $\int VdQ$ was calculated directly from the potential V versus $Q - Q_0$ curves at different constant temperatures. Hereafter, the results shown in Figures 4 and 5, and Equation 8 will be compared with those obtained by MDSC.

Braga et al. have observed glass transitions in[101,102,103], and Nomoto and Hanaya[104] have observed dipolar-glass transition by adiabatic calorimetry in $C_5NH_6(BF_4)_{1-x}(PF_6)_x$ solid solution. The temperature dependence τ for the relaxation times of fragile liquids is expressed by the Vogel-Tammann-Fulcher equation[105] by fitting,

$$\tau = A\, e^{\frac{B}{T - T_0}} \tag{8}$$

where A, B, and T_0 are empirical parameters and the expression provides the tendency of τ to diverge at a finite temperature T_0 (a temperature typically below T_g). The dipolar-glass transition was shown to be due to the thermally activated reorientation process of the electric dipoles. These results revealed once over that the dipolar-glass state is a non-equilibrium state where the rearrangement of the electric dipoles is frozen due to the slowdown of the thermally activated reorientation motion, as the temperature decreases; which reinforces the ε_r' dependence of the frequency at lower temperatures.

Figure 6a shows the molar heat capacity $C_{V'}$ and additional thermodynamic functions for $Na_{81}Cl_{27}O_{27}$ after optimization

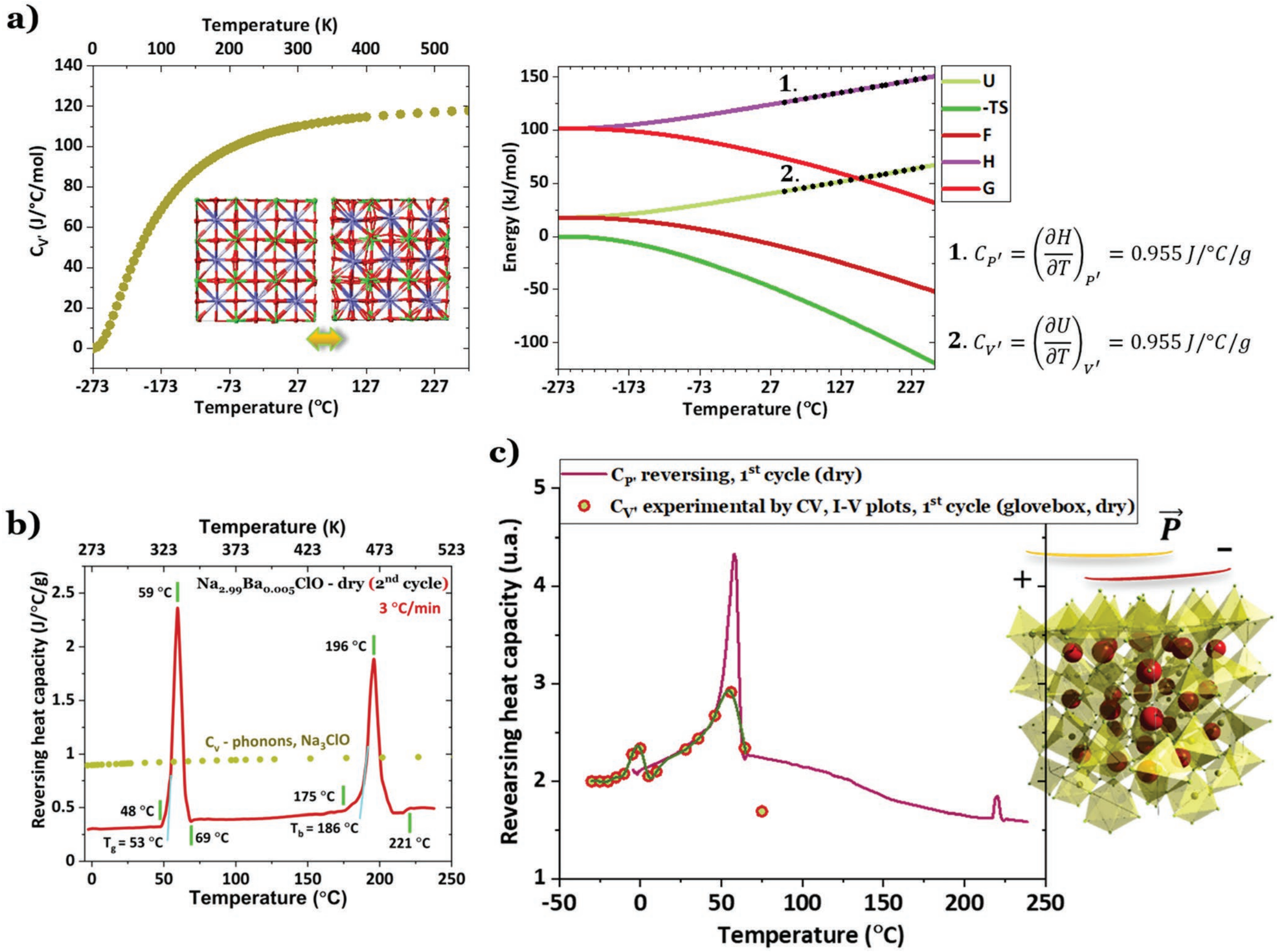

Figure 6. Temperature-dependent a) phonon simulated heat capacity and b) thermodynamic functions for the optimized Na_3ClO (sg. Pm-3m) after allowing the structure to relax at 56 °C using ab initio molecular dynamics. Temperature-modulated reversing heat capacity for $Na_{2.99}Ba_{0.005}ClO$ compared with b) phonon-calculated heat capacity for Na_3ClO and c) compared with the experimental data obtained by cyclic voltammetry (*I–V* plots) performed in the freezer of an Ar-filled glovebox, both corresponding to the first cycle (2 °C min^{-1}). Note: The polarization and amorphous characteristics are likely attained from thermally activated phonons a) and c) – right (octahedral – Li_6O, red atom – Cl).

of the crystalline structure, followed by molecular dynamics at 56 °C and phonon simulations. The goal was to obtain a structure that mimics the glass and freezes it to lower temperatures. The phonon dispersion (Figure S7, Supporting Information) shows imaginary frequencies likely corresponding to structural instabilities (2.39%) observed in another ferroelectric of the family, Li_3ClO, by neutron spectroscopy[106] and in ferroelectric perovskites[107,53].

Figure 6b,c shows the MDSC output and the dependence of the heat flux on the temperature; it is shown the normalization of the data to obtain the reversing heat flow that, after calibration with the sapphire, Equation 5. No anomalies due to free water and hydroxide phases are observed in the latter. The hydroxide phases release most water from 109–209 °C (Figure S5, Supporting Information). The reversing $C_{P'}$ shows all the temperature anomalies corresponding to the local minimum and maximum in Figure 5b. These similar anomalies were not only obtained with very different techniques but also with different samples, highlighting the reproducibility of the obtained results. The first samples correspond to poled asymmetric $Zn/Na_{2.99}Ba_{0.005}ClO/Cu$ cells (Figure 5b) ($A \approx 4 - 6$ cm^2, $d > 1$ mm, ≥ 1 g) and the second to $Na_{2.99}Ba_{0.005}ClO$ with < 20 mg (Figure 6) in an alumina crucible.

In summary, at 36 – 41 °C, the potential energy of the ferroelectric Na$^+$-glass in $Zn/Na_{2.99}Ba_{0.005}ClO/Cu$ cells evolves to a local minimum; at 46 – 48 °C, the potential energy achieves a metastable local maximum, correspondent to the depolarization temperature, where the maximum polarization changes from positive to negative (Figure 5a), which boosts the glass transition. At 56 – 58 °C, $Na_{2.99}Ba_{0.005}ClO$ is a "liquid" by transition from the glassy state. The transition at 186 – 217 °C is the Burn temperature (Figure 1 and Figure 6b,c), eventually affected by the presence of residual hydroxide phases (Figures S5 and S8, Supporting Information). The peak anomalies in Figure 6c likely correspond to lambda transitions characterized by a constant volume and a constant entropy.

3. Conclusion

The thermal anomalies in the quasi-adiabatic ferroelectric $Na_{2.99}Ba_{0.005}ClO$ were studied by EIS and CV (I–V curves) with symmetric Au/$Na_{2.99}Ba_{0.005}ClO$/Au and poled asymmetric Zn/$Na_{2.99}Ba_{0.005}ClO$/Cu cells, and by MDSC, TGA, and XRD in Al_2O_3 crucibles. Ab initio, DFT, molecular dynamics, and phonon simulations were also performed. All phase transitions and associated phenomena were observed independently, using the different methods based on electrical/ionic and thermodynamic indicators. The first transition above –10 °C is likely due to topologic phenomena related to the circulation of electrons in positive feedback, which is more expressive in the asymmetric cell. At 56 – 58 °C, the $Na_{2.99}Ba_{0.005}ClO$ is a supercooled liquid above the transition from glass initiated at 46 – 48 °C. The transition at 186 – 217 °C represents the Burn temperature that marks the beginning of the fully paraelectric state.

The free and hydroxide phases' water that may have been absorbed while manipulating the sample is fully eliminated in the second heating-cooling cycle under an inert gas flow (N_2).

As a ferroelectric, the Na^+-glass electrolyte is also a pyroelectric with huge pyroelectric coefficient that can reach $\frac{dP}{dT} = 5.37\ \mathrm{C\ m^{-2}\ °C^{-1}}$ [–5 °C,46 °C].

It is demonstrated that the $Na_{2.99}Ba_{0.005}ClO$ ferroelectric-electrolyte shows a depolarizing temperature traditionally attributed to the regular/relaxor ferroelectric transition. Conversely, at low temperatures, its dielectric constant is highly dependent on the frequency of the applied electric field, a feature that is usually attributed to relaxor ferroelectrics. The $Na_{2.99}Ba_{0.005}ClO$ glass electrolyte is shown to be a soft relaxor with very strong nonlinear dielectric and polarization properties; it can also be described as a superparaelectric, but above ≈ 25 °C, it shows enhanced quasi-adiabatic features. The polarization increases almost constantly with each added quasi-adiabatic cycle, reaching an increment of 28 C m^{-2}, corresponding to a capacitance of 70 F m^{-2}, and an energy of ≈5.6 J m^{-2} per cycle with amplitude $\Delta V = 0.2$ V at 20 °C. These quasi-adiabatic cycles show negative differential capacitance, as in emergent phenomenon, likely necessary not to encompass hysteresis. In asymmetric cells above –10 °C, a negative resistance is also observed; the latter is related to the negative capacitance and the circulation of electrons in positive feedback through the cell's surface that tunnel back to the negative electrode.

While the $Na_{2.99}Ba_{0.005}ClO$ ferroelectric-electrolyte shows features of a relaxor or a superparaelectric, its remanent polarization is giant and likely related with 1D long-range order chains that remain aligned with the applied electric field even after its action ceases. Yet, conversely to regular ferroelectrics, they can reverse their polarization with almost no energy cost.

The dipolar glass nanodomains that can be characterized by assessing electrical, thermodynamic, and structural properties may shed light on understanding fragile fractal glasses showing numerous thermally activated features and giant polarization with applications in energy harvesting and storage.

4. Experimental Section

Synthesis of $Na_{2.99}Ba_{0.005}ClO$ and Cells: The ferroelectric glass electrolyte' exceptional properties have been analyzed.[15,106]

The material under study in this work is the dry Na^+- glass electrolyte with enhanced ferroelectric and thermoelectric properties synthesized by water solvation, as presented by Braga et al.[108]. The all-solid-state electrolyte $Na_{2.99}Ba_{0.005}OCl_{1-x}(OH)_x$ was obtained from the commercial precursors NaCl (99.5%, ITW Reagents, PanReac AppliChem), Na(OH) (98.0%, LabKem), and $Ba(OH)_2$ (anhydrous, 94% – 98%, Alfa Aesar). Then, $Na_{2.99}Ba_{0.005}OCl_{1-x}(OH)_x$ was allowed to react and dry between 230 and 250 °C. After obtaining the dry $Na_{2.99}Ba_{0.005}ClO$ solid-state material, the electrolyte was ground for 40 min (300 rpm) using a ball milling machine with an Agate container and five balls with a diameter of 20 mm, which can be closed hermetically to avoid water absorption during the process.[17]

The Au/$Na_{2.99}Ba_{0.005}ClO$/Au and Zn/$Na_{2.99}Ba_{0.005}ClO$/Cu double-layer pouch cells had A = 6.25 cm^2 and electrolyte thicknesses from 1–4 mm (≥ 1 g).

Since $Na_{2.99}Ba_{0.005}ClO$ possesses exceptional characteristics, studying its thermal behavior using DSC and TGA techniques allowed us to understand its potential applications.

Temperature-Modulated Differential Scanning Calorimetry (MDSC) and Thermogravimetry Analysis (TGA): A TA Instruments, DSC model Discover 25 was used for performing MDSC with a temperature accuracy of ±0.1 °C and a temperature precision of ± 0.01 °C. Before the experiments, the equipment was calibrated. First, the indium was used in the sample crucible to check the calibration from –39.7 to 250.4 °C at 20.0 °C min^{-1} and later to determine $K_{C_p\,rev}$, the sapphire was used (from 0.00 to 237.61 °C at 3.00 °C min^{-1}), always with alumina crucibles. The gas used was nitrogen with a flow rate of 50 mL min^{-1}. More detail in Figures S4 –S6 (Supporting Information).

Thermogravimetric analysis (TGA) was performed to monitor the sample's variation in mass as a function of temperature and time. For this study, the model TGA 550 of the TA Instruments was used. The calibration and experiments were performed from room temperature to 260 °C at 5 °C min^{-1}. The crucibles used were alumina placed on a platinum pan (100 µL). The gas used was also nitrogen, with a flow rate of 100 mL min^{-1}. The samples used for both MDSC and TGA had > 20 mg.

Electrical Impedance Spectroscopy (EIS) and Cyclic Voltammetry (CV): For EIS, a Biologic VMP-300 impedance meter imposes a small amplitude AC signal to the cell's terminals. The AC potential difference and current response of the sample cell allow for determining the cells' impedance (resistive, capacitive, and inductive characteristics) and equivalent circuits related to their components at controlled frequencies. The EIS studies complemented the study of the cells. EIS was performed in the frequency range of 7 MHz to 0.1 Hz with an amplitude signal of 10 mV. Samples were studied in Au/$Na_{2.99}Ba_{0.005}ClO$/Au cells from 25 to 172 °C.

Cyclic Voltammetry (CV) is a DC electrochemical technique used to provide information about the cells' dynamic behavior while performing cycles under an imposed potential/electric field rate. CV measurements with the present cells were performed within the potential window of –6.0 to +6.0 V, –0.4 to –0.2 V, –0.2 to 0.2 V, –0.4 to 1.5 V and scan rates of 50 mV s^{-1} and 2 mV s^{-1}. Both Au/$Na_{2.99}Ba_{0.005}ClO$/Au and Zn/$Na_{2.99}Ba_{0.005}ClO$/Cu cells were used. The CV experiments from –35 to 28 °C were performed in an Ar-filled glovebox.

X-ray Diffraction: Variable-temperature Powder X-Ray Diffraction (PXRD) data were recorded on a PANalytical X'Pert Powder diffractometer (Cu-$K_{\alpha 1,2}$ X-radiation, $\lambda_1 = 1.540598$ Å; $\lambda_2 = 1.544426$ Å) under vacuum, equipped with a PIXcel 1D detector, a flat-plate sample holder in a Bragg–Brentano para-focusing optics configuration (40 kV, 50 mA), and a high-temperature Anton Paar HKL16 chamber controlled by an Anton Paar 100 TCU unit. Intensity data were collected in the continuous mode (ca. 100 s data acquisition) in the angular range ca. $5 \leq 2\theta(°) \leq 70$.

Ab Initio and Phonon Simulations: An ab initio molecular dynamics (AMD) as implemented in VASP[109] was used to simulate the Na_3ClO

structure at 56 °C, with a supercell $(Na_3ClO)_{27}$, after optimization of the crystalline structure (Pm-3m), according to the procedure described.[53] DFT simulations used Projector Augmented Wave (PAW) potentials in the Generalized Gradient Approximation (GGA)[110]. Electronic structure calculations were conducted with cut-off energy of 500 eV. The requested k-spacing was 0.25 Å^{-1}, which led to a 2 × 2 × 2 mesh. This corresponds to actual k-spacings of 0.237 × 0.236 × 0.234 Å^{-1}. AMD simulations for a canonical ensemble NV'T were performed with 4 fs time-steps to a maximum of 8 ps; velocities were rescaled to maintain a constant temperature using the Nosé's thermostat[111] with a mass chosen such that temperature fluctuates with a period of 40 time-steps. The NV'T was allowed to relax at least until decoherence was noticeably observed. AMD simulations were also performed with an isothermal-isobaric NP'T ensemble (constant number of atoms, pressure, and temperature).

Phonon simulations to determine the phonon dispersion, the density of states DOS, and thermodynamic functions[112] were carried out for the supercell $(Na_3ClO)_{27}$ at 56 °C (329 K) to obtain accurate functions near the glass transition for the disordered structure and at temperatures within the application range. Crystal structure design, VASP, and PHONON were used as implemented in MedeA version 3.2.2.

Signal Analysis: The total heat flow signal $\left(\frac{dH}{dt}\right)$ in the MDSC was obtained from the average value of the determined modulated heat flow signal by Fourier transform analysis. For the analysis of the heat flux variation with the temperature, a mathematical model is used based on the block heat capacity method, where a thermal system is represented by thermal resistances and heat capacities[65,66,113,114]. The software used was TRIOS from TA-Instruments, and the sample interval was 0.1 s/pt. The data file corresponding to the plot of Figure 6b contains 52100 points.

Statistical Analysis: All data plotting, differentiation, integration, and interpolation to obtain $C_{V'}$ correspondent to I–V curves at different temperatures in Figure 6c, and fitting in Figure 6a, were performed using OriginPro 2020b. The AFM, and SKP data were obtained with Biologic M470 version 1.47.5951. EIS, CV, and polarization P versus V was obtained directly from $Q - Q_0$ versus V displayed by Biologic EC-lab® software version V11.40. No statistical analysis was performed with the presented samples.

Supporting Information

Supporting Information is available from the Wiley Online Library or from the author.

Acknowledgements

M.H.B. acknowledges Professor John B. Goodenough's endowment to the MatER – Materials for Energy Research lab, FEUP. The authors thank Rosário Soares for assistance with PXRD measurements. This work was supported by the CAVALI project, with reference POCI-01-0247-FEDER-047728, co-funded by the ERDF, through the COMPETE 2020, under the PORTUGAL 2020 Partnership Agreement; the Portuguese Foundation for Science and Technology FCT UIDP/50 022/2020 Emerging Technologies – LAETA and PTDC/QUI-ELT/2593/2021 "Redox-active Metal-Organic Frameworks as Electrode Materials for Lithium-Ion Batteries" projects, the ALBATTS ERASMUS+ 612675-EPP-1-2019-1-SE-EPPKA2-SSA-B co-funded by the Erasmus Program of the European Union and FLY.PT—Mobilize the Portuguese aviation industry to disrupt the future urban air transport project, co-funded by the ERDF through Portugal 2020. This work has also received funding from the European Research Council (ERC) under the European Union's Horizon Europe Framework Programme, ERC-2021-Starting Grant, grant agreement no. 101039748-ELECTROCOFS.

Conflict of Interest

The authors declare no conflict of interest.

Author Contributions

Experiments: M.C.B., A.A., and M.H.B.; specific review of state of the art: M.C.B., H.K., A.A., B.A.M., and M.S.; technical contributions and overview: M.S.; conceptualization, formal analysis, simulations, and supervision: M.H.B.; original draft, review, and editing: All. All authors have read and agreed to the published version of the manuscript.

Data Availability Statement

The data that support the findings of this study are available from the corresponding author upon reasonable request.

Keywords

adiabatics, energy harvesting, energy storages, ferroelectrics, polar chains, relaxors, solid electrolytes, superparaelectrics, topologic insulators

Received: October 26, 2022
Revised: November 18, 2022
Published online:

---

[1] G. Mutezo, J. Mulopo, *Renewable Sustainable Energy Rev.* **2021**, *137*, 110609.
[2] M. M. Rahman, N. Sultana, E. Velayutham, *Renewable Energy* **2022**, *184*, 252.
[3] J. Đurašković, M. Konatar, M. Radović, *Energy Rep.* **2021**, *7*, 481.
[4] M. W. Zafar, M. Shahbaz, F. Hou, A. Sinha, *J. Cleaner Prod.* **2019**, *212*, 1166.
[5] P. Saini, L. Gidwani, *J. Energy Storage* **2022**, *45*, 103493.
[6] Y. Yang, S. Bremner, C. Menictas, M. Kay, *Renewable Sustainable Energy Rev.* **2018**, *91*, 109.
[7] J. Biemolt, P. Jungbacker, T. van Teijlingen, N. Yan, G. Rothenberg, *Materials* **2020**, *13*, 425.
[8] F. Danzi, P. P. Camanho, M. H. Braga, *Molecules* **2021**, *26*, 5226
[9] C. W. Wu, X. Ren, W. X. Zhou, G. Xie, G. Zhang, *APL Mater.* **2022**, *10*, 040902
[10] F. Lv, Z. Wang, L. Shi, J. Zhu, K. Edström, J. Mindemark, S. Yuan, *J. Power Sources* **2019**, *441*, 227175.
[11] J. B. Goodenough, M. H. Braga, *Dalton Trans.* **2018**, *47*, 645.
[12] Z. Cheng, T. Liu, B. Zhao, F. Shen, H. Jin, X. Han, *Energy Storage Mater.* **2021**, *34*, 388.
[13] L. Yue, J. Ma, J. Zhang, J. Zhao, S. Dong, Z. Liu, G. Cui, L. Chen, *Energy Storage Mater.* **2016**, *5*, 139.
[14] Y. Meesala, A. Jena, H. Chang, R. S. Liu, *ACS Energy Lett.* **2017**, *2*, 2734.
[15] M. H. Braga, J. E. Oliveira, T. Kai, A. J. Murchison, A. J. Bard, J. B. Goodenough, *J. Am. Chem. Soc.* **2018**, *140*, 17968.
[16] A. N. Guerreiro, B. A. Maia, H. Khalifa, M. C. Baptista, M. H. Braga, *Batteries* **2022**, *8*, 232.
[17] F. Danzi, M. Valente, S. Terlicka, M. H. Braga, *APL Mater.* **2022**, *10*, 031111.
[18] W. Zhang, Y. Liu, Z. Guo, *Sci. Adv.* **2019**, *5*, 7412.
[19] E. A. Il'ina, A. A. Raskovalov, A. P. Safronov, *Thermochim. Acta* **2017**, *657*, 26.

[20] J. Han, M. He, M. Yang, Q. Han, F. Wang, F. Zhong, M. Xu, Q. Li, H. Zhu, C. Shan, W. Hu, X. Chen, X. Wang, J. Gou, Z. Wu, J. Wang, *Light: Sci. Appl.* **2020**, *91*, 167.

[21] L. Yang, X. Kong, F. Li, H. Hao, Z. Cheng, H. Liu, J.-F. Li, S. Zhang, *Prog. Mater. Sci.* **2019**, *102*, 72.

[22] K. Zou, Y. Dan, H. Xu, Q. Zhang, Y. Lu, H. Huang, Y. He, *Mater. Res. Bull.* **2019**, *113*, 190

[23] Z. Liu, T. Lu, J. Ye, G. Wang, X. Dong, R. Withers, Y. Liu, *Adv. Mater. Technol.* **2018**, *3*, 1800111.

[24] B. Luo, X. Wang, E. Tian, H. Song, H. Wang, L. Li, *ACS Appl. Mater. Interfaces* **2017**, *9*, 19963.

[25] B. Chu, X. Zhou, K. Ren, B. Neese, M. Lin, Q. Wang, F. Bauer, Q. M. Zhang, *Science* **2006**, *313*, 334.

[26] X. Hao, *J. Adv. Dielectr.* **2013**, *03*, 1330001.

[27] J. H. Tortai, N. Bonifaci, A. Denat, C. Trassy, *J. Appl. Phys.* **2005**, *97*, 053304.

[28] M. Rabuffi, G. Picci, *IEEE Trans. Plasma Sci.* **2002**, *30*, 1939.

[29] X. Hao, J. Zhai, X. Yao, *J. Am. Ceram. Soc.* **2009**, *92*, 1133.

[30] J. Parui, S. B. Krupanidhi, *Appl. Phys. Lett.* **2008**, *92*, 192901.

[31] R. M. Wallace, G. Wilk, *MRS Bull.* **2002**, *27*, 186.

[32] G. D. Wilk, R. M. Wallace, J. M. Anthony, *J. Appl. Phys.* **2001**, *89*, 5243.

[33] X. Liu, S. Xue, J. Ma, J. Zhai, B. Shen, F. Wang, X. Zhao, H. Yan, *J. Eur. Ceram. Soc.* **2018**, *38*, 4631.

[34] L. Kumar Pradhan, M. Kar, *Multifunctional Ferroelectric Materials*, IntechOpen, London **2021**.

[35] F. Li, S. Zhang, D. Damjanovic, L.-Q. Chen, T. R. Shrout, *Adv. Funct. Mater.* **2018**, *28*, 1801504.

[36] J. Wu, A. Mahajan, L. Riekehr, H. Zhang, B. Yang, N. Meng, Z. Zhang, H. Yan, *Nano Energy* **2018**, *50*, 723.

[37] L. Eric Cross, *Ferroelectrics* **1987**, *76*, 241.

[38] C. W. Ahn, C. -H. Hong, B. -Y. Choi, H. -P. Kim, H. -S. Han, Y. Hwang, W. Jo, K. Wang, J. -F. Li, J. -S. Lee, I. W. Kim, *J. Korean Phys. Soc.* **2016**, *68*, 1481.

[39] D. Viehland, S. J. Jang, L. E. Cross, M. Wuttig, *J. Appl. Phys.* **1990**, *68*, 2916.

[40] H. Qian, L. A. Bursill, *Int. J. Mod. Phys. B* **1996**, *10*, 2007.

[41] N. Qu, H. Du, X. Hao, *J. Mater. Chem. C* **2019**, *7*, 7993.

[42] L. Yang, X. Kong, Z. Cheng, S. Zhang, *J. Mater. Chem. A* **2019**, *7*, 8573.

[43] F. Li, J. Zhai, B. Shen, X. Liu, K. Yang, Y. Zhang, P. Li, B. Liu, H. Zeng, *J. Appl. Phys.* **2017**, *121*, 054103.

[44] L. K. Pradhan, R. Pandey, M. Kar, *J. Phys.: Condens. Matter* **2019**, *32*, 045404.

[45] D. Alikin, A. Turygin, A. Kholkin, V. Shur, *Materials* **2017**, *10*, 47.

[46] H. Pan, S. Lan, S. Xu, Q. Zhang, H. Yao, Y. Liu, F. Meng, E.-J. Guo, L. Gu, D. Yi, X. R. Wang, H. Huang, J. L. MacManus-Driscoll, L. -Q. Chen, K. -J. Jin, C. -W. Nan, Y. -H. Lin, *Science* **2021**, *374*, 100.

[47] J. Kim, S. Saremi, M. Acharya, G. Velarde, E. Parsonnet, P. Donahue, A. Qualls, D. Garcia, L. W. Martin, *Science* **2020**, *369*, 81.

[48] B. Neese, B. Chu, S. G. Lu, Y. Wang, E. Furman, Q. M. Zhang, *Science* **2008**, *321*, 821.

[49] S. Nomura, K. Uchino, R. E. Newnham, *Ferroelectrics* **1980**, *23*, 187.

[50] S. E. Park, T. R. Shrout, *J. Appl. Phys.* **1997**, *82*, 1804.

[51] Q. M. Zhang, V. Bharti, X. Zhao, *Science* **1998**, *280*, 2101.

[52] Z. Kutnjak, J. Petzelt, R. Blinc, *Nature* **2006**, *441*, 956.

[53] M. H. Braga, *Materials* **2021**, *14*, 2398.

[54] J. Bisquert, A. Guerrero, *J. Am. Chem. Soc.* **2022**, *144*, 5996.

[55] E. V. Colla, E. Y. Koroleva, N. M. Okuneva, S. B. Vakhrushev, *J. Phys. Condens.: Matter* **1992**, *4*, 3671.

[56] L. E. Cross, *Ferroelectrics* **1994**, *151*, 305.

[57] G. Burns, F. H. Dacol, *Solid State Commun.* **1983**, *48*, 853.

[58] I. W. Chen, *J. Phys. Chem. Solids* **2000**, *61*, 197.

[59] Y. Xi, C. Zhili, L. E. Cross, *J. Appl. Phys.* **1998**, *54*, 3399.

[60] J. C. W. Folmer, S. Franzen, *J. Chem. Educ.* **2003**, *80*, 813.

[61] M. Reading, D. J. Hourston, *Modulated-Temperature Differential Scanning Calorimetry: Theoretical and Practical Applications in Polymer Characterisation*, Springer, Dordrecht, Netherlands **2006**.

[62] Hitachi, *Introducing the Temperature Modulated DSC*, High-Tech Science Corporation, Tokyo, Japan **1993**, *64*.

[63] H. Qian, X. Hongde, W. Kai, L. Rongbin, R. Xiaoning, Z. Li, Y. Penghui, *Chem. Thermodyn. Therm. Anal.* **2022**, *6*, 100040.

[64] L. C. Thomas, "Modulated DSC ® Paper #3 Modulated DSC ® Basics; Optimization of MDSC ® Experimental Conditions," TA Instruments, **2005**.

[65] L. C. Thomas, "Modulated DSC ® Paper #2 Modulated DSC ® Basics; Calculation and Calibration of MDSC ® Signals," TA Instruments, **2005**.

[66] L. Thomas, "Modulated DSC® Paper# 1 Why modulated DSC®?; an overview and summary of advantages and disadvantages relative to traditional DSC," TA Instruments, **2005**.

[67] C. A. Angell, K. L. Ngai, G. B. McKenna, P. F. McMillan, S. W. Martin, *J. Appl. Phys.* **2000**, *88*, 3113.

[68] S. Kojima, V. N. Novikov, M. Kodama, *J. Chem. Phys.* **2000**, *113*, 6344.

[69] N. Li, J. D. Perea, T. Kassar, M. Richter, T. Heumueller, G. J. Matt, Y. Hou, N. S. Güldal, H. Chen, S. Chen, S. Langner, M. Berlinghof, T. Unruh, C. J. Brabec, *Nat. Commun.* **2017**, *8*, 14541.

[70] J. Drzeżdżon, D. Jacewicz, A. Sielicka, L. Chmurzyński, *TrAC, Trends Anal. Chem.* **2019**, *110*, 51.

[71] B. Wunderlich, *Prog. Polym. Sci.* **2003**, *28*, 383.

[72] F. Cser, F. Rasoul, E. Kosior, *J. Therm. Anal. Calorim.* **1998**, *52*, 293.

[73] F. Cser, J. Hopewell, E. Kosior, *J. Therm. Anal. Calorim.* **2004**, *53*, 493.

[74] F. Cser, R. A. Shanks, *J. Therm. Anal. Calorim.* **2004**, *54*, 637.

[75] A. Scoppio, D. Cavallo, A. J. Müller, D. Tranchida, *Polym. Test.* **2022**, *113*, 107656.

[76] K. L. Sahoo, R. Sahu, *J. Non-Cryst. Solids* **2013**, *365*, 33.

[77] J. McHugh, P. Fideu, A. Herrmann, W. Stark, *Polym. Test.* **2010**, *29*, 759.

[78] P. Boolchand, W. J. Bresser, *Nature* **2001**, *410*, 1070.

[79] C. Holbrook, "Characterization and Solid Electrolyte behavior of (Ag2S)x(As2S3)1-x glasses," **2007**.

[80] Z. Cheng, B. Zahiri, X. Ji, C. Chen, D. Chalise, P. V. Braun, D. G. Cahill, *Small* **2021**, *17*, 2101693.

[81] O. Checa, E. Olaya, J. E. Diosa, R. A. Vargas, *Microelectronics J.* **2008**, *39*, 1274.

[82] M. Cui, P. S. Lee, *Chem. Mater.* **2016**, *28*, 2934.

[83] R. Vijaya Kumar, C. Srinivasu, K. Siva Kumar, *Solid State Sci.* **2011**, *13*, 379.

[84] R. Richert, *J. Chem. Phys.* **2011**, *134*, 144501.

[85] D. Rosenbach, T. W. Schmitt, P. Schüffelgen, M. P. Stehno, C. Li, M. Schleenvoigt, A. R. Jalil, G. Mussler, E. Neumann, S. Trellenkamp, A. A. Golubov, A. Brinkman, D. Grützmacher, T. Schäpers, *Sci. Adv.* **2021**, *7*, 1854.

[86] L. Esaki, *Phys. Rev.* **1958**, *109*, 603.

[87] L. Esaki, *Rev. Mod. Phys.* **1974**, *46*, 237.

[88] K. Kim, J. Jang, H. Kim, *Results Phys.* **2021**, *25*, 104279.

[89] W. T. H. Koch, R. Munser, W. Ruppel, P. Würfle, *Ferroelectrics* **2011**, *13*, 305.

[90] J. Starkiewicz, L. Sosnowski, O. Simpson, *Nature* **1946**, *158*, 28.

[91] Z. Fan, W. Ji, T. Li, J. Xiao, P. Yang, K. P. Ong, K. Zeng, K. Yao, J. Wang, *Acta Mater.* **2015**, *88*, 83.

[92] Y. Tokura, M. Kawasaki, N. Nagaosa, *Nat. Phys.* **2017**, *13*, 1056.

[93] S. Varigonda, T. T. Georgiou, *IEEE Trans. Autom. Control* **2001**, *46*, 65.

[94] H. J. Lee, J. Y. Jo, *Electron. Mater. Lett.* **2019**, *15*, 297.

[95] M. Hoffmann, S. Salahuddin, *MRS Bull.* **2021**, *46*, 930.

[96] K. Srikanth, S. Patel, R. Vaish, *Int. J. Appl. Ceram. Technol.* **2018**, *15*, 546.

[97] R. V. K. Mangalam, J. C. Agar, A. R. Damodaran, J. Karthik, L. W. Martin, *ACS Appl. Mater. Interfaces* **2013**, *5*, 13235.
[98] M. E. Edwards, A. K. Batra, A. K. Chilvery, P. Guggilla, M. Curley, M. D. Aggarwal, *Mater. Sci. Appl.* **2012**, *3*, 851.
[99] B. K. Ng, T. S. Velayutham, W. C. Gan, W. H. Abd Majid, V. Periasamy, R. Hashim, N. I. Mat Zahid, *Ferroelectrics* **2013**, *445*, 67.
[100] P. Charbonneau, J. Kurchan, G. Parisi, P. Urbani, F. Zamponi, *Nat. Commun.* **2014**, *5*, 3725.
[101] M. H. Braga, J. A. Ferreira, A. J. Murchison, J. B. Goodenough, *J. Electrochem. Soc.* **2017**, *164*, A207.
[102] M. H. Braga, J. E. Oliveira, T. Kai, A. J. Murchison, A. J. Bard, J. B. Goodenough, *J. Am. Chem. Soc.* **2018**, *140*, 17968.
[103] M. H. Braga, J. E. Oliveira, A. J. Murchison, J. B. Goodenough, *Appl. Phys. Rev.* **2020**, *7*, 011406.
[104] M. Nomoto, M. Hanaya, *Thermochim. Acta* **2020**, *683*, 178441.
[105] E. Courtens, *Phys. Rev. Lett.* **1984**, *52*, 69.
[106] M. H. Braga, J. A. Ferreira, V. Stockhausen, J. E. Oliveira, A. El-Azab, *J. Mater. Chem. A* **2014**, *2*, 5470.
[107] G. Pilania, T. Lookman, *Phys. Rev. B* **2014**, *90*, 115121.
[108] M. H. Braga, A. J. Murchison, J. A. Ferreira, P. Singh, J. B. Goodenough, *Energy Environ. Sci.* **2016**, *9*, 948.
[109] G. Kresse, J. Furthmüller, *Phys. Rev. B* **1996**, *54*, 11169.
[110] J. P. Perdew, Y. Wang, *Phys. Rev. B* **1992**, *45*, 13244.
[111] N. Shuichi, *Prog. Theor. Phys. Suppl.* **1991**, *103*, 1.
[112] K. Parlinski, Z. Q. Li, Y. Kawazoe, *Phys. Rev. Lett.* **1997**, *78*, 4063.
[113] R. L. Danley, *Thermochim. Acta* **2002**, *395*, 201.
[114] L. C. Thomas, “Modulated DSC ® Paper #3 Modulated DSC ® Basics; Optimization of MDSC ® Experimental Conditions”, TA.